V International Conference on Computational Methods for Coupled Problems in Science and Engineering
COUPLED PROBLEMS 2013
S. Idelsohn, M. Papadrakakis and B. Schrefler (Eds)

# NUMERICAL ANALYSIS OF THE COUPLING BETWEEN MECHANICAL STRAIN AND THERMAL CONDUCTIVITY OF CERAMIC MATRIX COMPOSITES.

**DAVID R. HAYHURST**

School of Mechanical, Aerospace, & Civil Engineering,
The University of Manchester, George Begg Building C-004,
MANCHESTER, M13 9PL, U.K.
e-mail: d.r.hayhurst@manchester.ac.uk

**Key words:** Ceramic matrix composites, Tows, Unit cell, 0-90 woven composites, Stress-strain response. Thermal conductivity degradation, Damage mechanisms,

**Abstract.** The paper addresses the numerical modeling of the coupling between mechanical strain and thermal conductivity in Ceramic Matrix Composites {CMCs} when subjected to uni-axial mechanical straining.

A computationally economic finite element-based multi-linear elastic orthotropic mechanical materials description combined with a multi-linear discretisation of thermal conductivity-strain response has been developed to predict the stress-strain, fracture, and thermal conductivity-strain behaviour of a ceramic matrix composites with strain-induced damage. The finite element analysis utilises a solid element to represent an homogenised orthotropic medium of a heterogeneous uni-directional tow. The discretised non-linear multi-axial stress-strain curves and non-linear multi-axial strain dependent thermal behaviour have been implemented by a user defined subroutine in the commercial finite element package ABAQUS. The model has been used to study the performance of a carbon fibre/carbon matrix-SiC matrix (C/C-SiC) plain weave laminate DLR-XT. With the effects of fibre waviness included, the global stress-strain curves, with catastrophic fracture behaviour, and the thermal conductivity-strain response have been predicted. Excellent comparisons have been made between predictions and experimental data, with fibre waviness included.

## 1 INTRODUCTION

The superior material properties of Ceramic Matrix Composites (CMCs), e.g. low density and good mechanical and thermal properties at high temperatures, make them favourable materials for use in: rocket nozzles; thermal protection systems; and gas turbine engines [1]. Increased operating temperatures, from 900-1200ºC for coated metallic superalloys to above 1300ºC, for CMCs, have the potential to achieve higher thermal efficiencies and lower emissions [2]. The economic use of CMCs in engineering components and structures requires an ability to simulate the material, and the component response at both the design and manufacturing stages [3]. To perform optimal design of these CMC engineering components, an efficient yet computationally accurate model is a necessary requirement.

The present paper addresses the development of a conceptually simple and computationally economic finite element, FE, technique, which emphasises the effects of

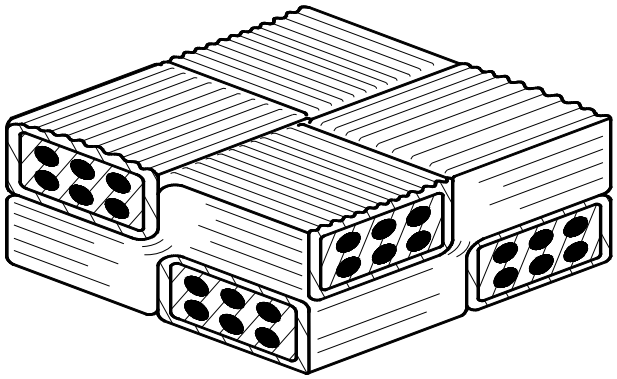

**Figure 1:** Schematic of a DLR-XT unit cell comprised of four tows.

strain-induced damage modes and their interactions on the mechanical behaviour. The approach adopted by [4] of modelling the composite using tows, i.e. a collection of thousands of fibres embedded in at least one matrix, has been adopted here. The tow is captured in a single orthotropic finite element, and the approach used to model the multi-axial stress-strain response, and property degradation for 0º/90º plain weave composites.

The DLR–XT, 10 high plain weave laminae [5], has been previously studied; and, an idealised unit cell of the material, that includes four tows, is shown schematically in Fig.1.

## 2 MECHANICAL BEHAVIOUR OF A UNI-DIRECTIONAL CMC TOW

Damage modes and their interactions on the stress-strain response are now introduced.

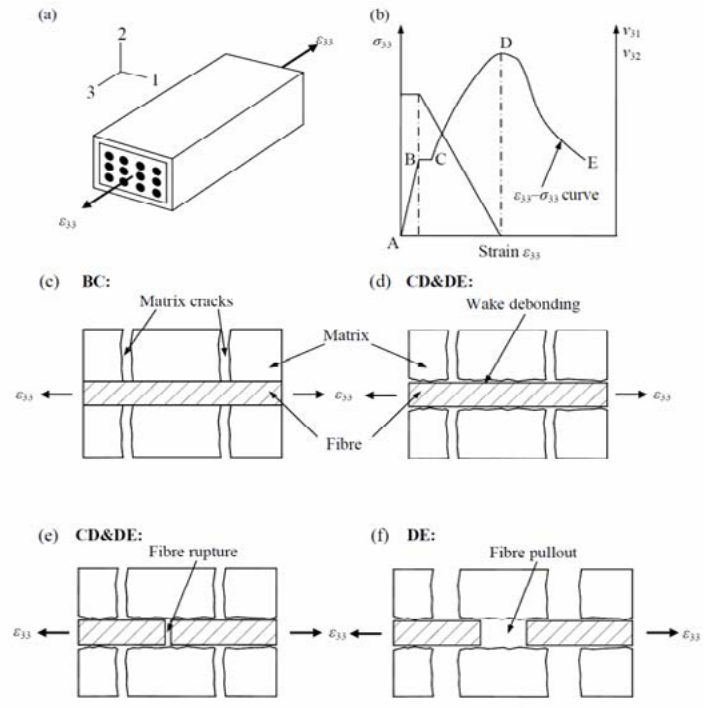


**Figure 2:** Schematic drawings of: (a) a uni-directional tow under longitudinal extension; (b) longitudinal stress-strain and Poisson's ratio-strain curves; and (c)–(f) corresponding damage modes.

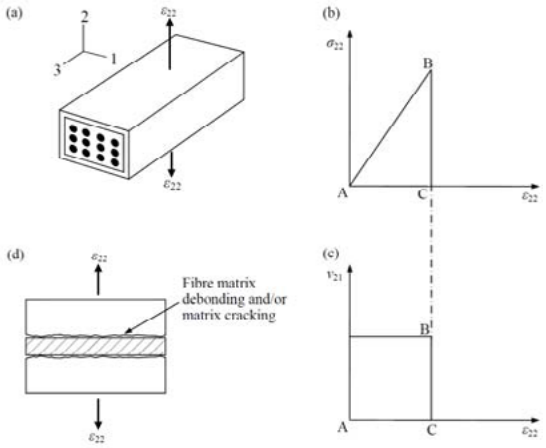


**Figure 3:** Schematic drawings of: (a) a uni-directional tow under transverse straining; (b) and (c) transverse stress-strain and Poisson's ratio curves; and (d) schematic of corresponding damage modes.

### 2.1 Longitudinal stress-strain response

When a uni-directional fibre-reinforced ceramic matrix composite tow undergoes uniform straining along the fibre direction, Fig.2a, it exhibits the longitudinal stress-strain response of Fig.2b [6]. Four characteristic stages in the stress-strain curve are [4]: **AB**: linear elastic material; **BC**: periodic matrix cracking occurs, Fig.2c; **CD**: fibre-matrix interface debonding and wake debonding, Fig.2d; and weaker fibre failure, Fig.2e; **DE**: the majority of fibres fail and are pulled out against the frictional stress along the wake debonding interface, Fig.2f. Figure 2b shows the variation of Poisson's ratio with longitudinal strain.

### 2.2 Transverse stress-strain response

When a uni-directional tow is subjected to transverse extension, Fig.3a, the material response is assumed to be linear elastic. The transverse Young's modulus, defined in Fig.3b, and the Poisson's ratio, $v_{21}$ shown in Fig.3c, are constant until the fibre-matrix debonding and/or matrix cracking take place, Fig.3d, at which point the damage is instantaneous and causes complete loss in strength, and the stress immediately drops to zero [7].

### 2.3 Shear stress-strain response

The shear stress-strain response, Fig.4a, is similar to the transverse response. The shear stress increases linearly with the shear strain Fig.4b, until a critical value is reached, when catastrophic shear failure, Fig.4c, occurs, and the shear stress immediately drops to zero, [8].

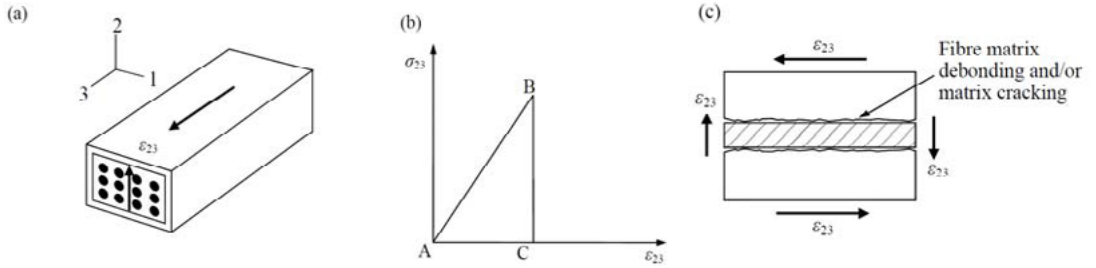


**Figure 4:** (a) a uni-directional tow under shear; (b) shear stress-strain curve; and (c) damage modes.

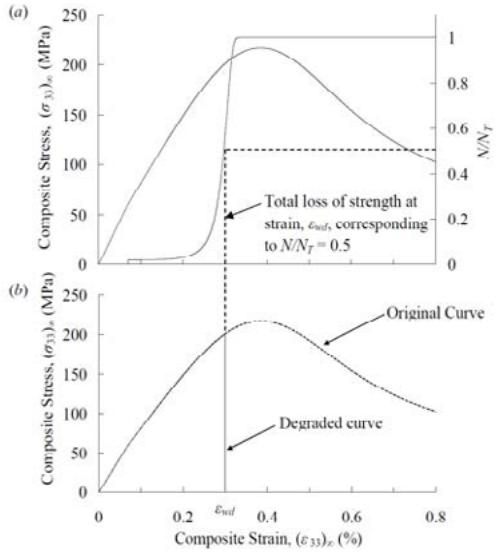


**Figure 5:** (a) stress-strain curve of a uni-directional tow under longitudinal loading and variation of normalised number of wake debonded blocks $N/N_T$ with composite strain $(\varepsilon_{33})_\infty$; and (b) stress-strain curve of a uni-directional tow under multi-axial loading. [8].

## 2.4 Longitudinal stress-strain response under multi-axial loading

When a uni-directional tow is subjected to two or more uni-axial loading cases, e.g. longitudinal, transverse, and shear loading, the effects of transverse tension or shear stress on the longitudinal stress-strain response are reflected in CMC experiments [5] addressed here.

For a uni-directional tow under longitudinal uni-axial loading, the material exhibits ductile behaviour, demonstrated as the gentle decreasing stress-strain curve after the peak in Fig.2b and Fig.5a [8]. This is due to the fibre-matrix interface wake debonding that occurs gradually, and creates a partially intact interface, which allows a failed fibre to pull out against the frictional stress along the wake debonding interface. It takes place within individual blocks, where a block is defined by a single fibre and matrix between two adjacent matrix cracks [4]. The variation of the normalised number of wake debonded blocks, $N$ with respect to the total number of blocks $N_T$ in a tow ($N/N_T$), with composite strain, $(\varepsilon_{33})_\infty$, is shown in Fig.5a. A positive transverse stress or a shear stress advances wake debonding, and also degenerates the partially intact interface to a fully separated gap. Hence the frictional stress reduces to zero and the pullout mechanism is then deactivated.

Even though the pullout mechanism is negated, it cannot explain the catastrophic fibre failure observed in the experiments [5]. Another mechanism, ***dynamic fibre failure by instantaneous pullout deactivation*** [8], is responsible for this brittle failure. The mechanism is that approximately one half of all blocks in a tow ($N/N_T = 0.5$, at the strain $\varepsilon_{wd}$ shown in Fig.5a simultaneously undergo instantaneous wake debonding and fibre pullout deactivation. By virtue of the way in which a ductile CMC is designed, the average wake debonding strain, $\varepsilon_{wd}$, is slightly less than the peak composite strain, and hence at this point the fibres are stressed to a high fraction of the average fibre failure stress. When the mechanism is triggered, a shear stress wave travels from the matrix cracks associated with the block; this induces a tension stress wave in the fibre to maintain equilibrium. The two tension waves

meet in the fibre at the centre of the block, and reflect as a wave with twice the amplitude of the incident wave. This doubling of the tensile stresses in the fibres therefore causes complete failure of the tow. By using this mechanism, the original curve, Fig.5b, switches to the degraded curve, which is for a tow subjected to multi-axial loading.

The variation of transverse, shear and axial tow properties with tow axial strain are assumed to fall to zero at failure. This dynamic failure is consonant with experimentally observed behaviour [5]. The transverse, and shear properties may not immediately drop to zero at failure; however, the worst condition of brittle failure has been assumed.

## 3 FORMULATION OF THE FINITE ELEMENT MODEL

A uni-directional tow is chosen to be the basic constituent in the FE model, and therefore an entire tow can be represented by a single 8-node solid finite element. This can be seen in Fig.2a where the 8 corners define the nodes. The material properties are assumed to be multi-linear elastic and the stress-strain and Poisson's ratios-strain curves, shown in Figs.2, 3 and 4, are used in the constitutive equations. The FE package ABAQUS, SIMULIA [9] with a user-defined subroutine UMAT is used to carry out the simulation.

### 3.1 Homogenisation of a uni-directional tow.

A heterogeneous uni-directional tow or lamina is homogenised to a single block which has the same overall dimensions and equivalent orthotropic material properties. There are nine independent material properties: Young's moduli: $E_3$, $E_2$, and $E_1$; Poisson's ratios: $v_{31}$, $v_{32}$, and $v_{12}$; and, Shear moduli: $G_{12}$, $G_{23}$, and $G_{13}$.

### 3.2 Discretisation of the stress-strain curve and constitutive equations

In order to perform a finite element analysis, the non-linear longitudinal stress-strain relationship is discretised to a multi-linear curve. The loading is imposed in terms of the displacement boundary conditions. The applied displacement is divided into many small increments. For each increment, the constitutive equation for an orthotropic material is [7]:

$$\{\Delta\boldsymbol{\sigma}\} = [\mathbf{C}(\Delta\boldsymbol{\varepsilon})]\{\Delta\boldsymbol{\varepsilon}\}; \tag{1}$$

$\{\Delta\boldsymbol{\sigma}\}$ and $\{\Delta\boldsymbol{\varepsilon}\}$ are the incremental stress and strain vectors, and $[\mathbf{C}(\Delta\boldsymbol{\varepsilon})]$ is the stiffness matrix.

### 3.3 Assumption made for the activation of catastrophic fracture failure

To activate dynamic fibre failure by instantaneous pullout deactivation, Fig.5b, two assumptions are made: (a) the switch from the original stress-strain curve to the degraded curve occurs by a small finite positive transverse stress, or by a small shear stresses; and (b) as a consequence, the Poisson's ratios, $v_{31}$ and $v_{32}$ start to decrease at the matrix cracking strain, and fall to zero at, $\varepsilon_{wd}$ in Fig.5a; as opposed to the peak load strain at D, in Fig.2b.

### 3.4 UMAT implementation in ABAQUS SIMULIA [9]

The multi-axial elastic properties, the constitutive equations, and the catastrophic failure activation are defined in the ABAQUS UMAT. For every increment, the UMAT reads the strains at each material point and then assigns the corresponding Young's moduli, Poisson's ratios and shear moduli. The constitutive equations are then used to update the stress fields. Solution-dependent state variables, STATEV, record different damage modes and control

their interactions. Automatic incrementation algorithms and redefinition variable, PNEWDT, are updated to ensure the discretised points are located exactly at the end of the increments.

Nine state variables are used to record the respective damage states associated with the nine material properties. The initial values of state variables, STATEV, are set to be 0. When the damage state changes, i.e. transverse cracking, shear failure, or dynamic fibre failure occurs, their corresponding STATEV value is set to be 1. The STATEV values associated with the Poisson's ratios, $v_{31}$ and $v_{32}$, are controlled by dynamic fibre failure. Once STATEV values are equal to 1, the material properties become a very small finite value, no matter what the local strains are. In the UMAT, the Jacobian matrix for mechanical loading is required and the expressions used for the current constitutive equation (Equation (1)) are given in [7].

### 3.5 Load path algorithm

Post-peak behaviour of composites and the associated loss of uniqueness, can pose a problems. This leads to zones of composite unloading with adjacent loading zones, whilst both zones are subjected to increasing strain, hence compatibility can be satisfied whilst equilibrium may be violated. The author has developed an approach that identifies the load-path within each tow that links many finite elements, and ensures that lines of force have continuity through the unit cell. Failure in one tow location is automatically transmitted along the tow in a way that ensures satisfaction of both compatibility and equilibrium.

To model the catastrophic dynamic fibre failure mechanism, load paths have been introduced into the FE analysis. A load path consists of a series of elements which form a continuous tow or lamina. It is assumed that: **(a)** In a load path, once the local longitudinal strain of any integration point (master point) reaches 90% of the wake debonding strain, $\varepsilon_{wd}$, the Poisson's ratios, $v_{31}$ and $v_{32}$, of all the other integration points (slave points) in this load path decrease proportionally with the reduction in the corresponding variable at the master point. The Poisson's ratios, $v_{31}$ and $v_{32}$, of all the integration points reduce to zero when the longitudinal strain of the master point reaches the wake debonding strain, $\varepsilon_{wd}$. **(b)** After that, elements in all load paths fail simultaneously and all their stress components unload to zero. The unloading slope is chosen to be as steep as possible, but consistent with maintaining numerical stability.

### 3.6 Implementation of the incremental constitutive law

For each FE increment, the constitutive law [7] has been implemented as follows:

1) Determine the material properties from the local strains and the multi-linear curves.
2) Identify the damage state and update the state variable, STATEV. If the dynamic fibre failure criterion is satisfied, then the load path algorithm is activated.
3) Update the stress increments using the incremental constitutive equations.
4) Update the material Jacobian matrix using equation [7].

## 4 MECHANICAL BEHAVIOUR OF PLANE WEAVE DLR-XT COMPOSITES

This section addresses the prediction of the stress-strain response of a plain weave DLR-XT composite, Fig.1, under uni-axial straining along the 0º tows. Effects of the tow waviness on the overall stress-strain curve of the composite are modelled. The material properties of the tow are used as input data to predict the overall mechanical behaviour of the composite.

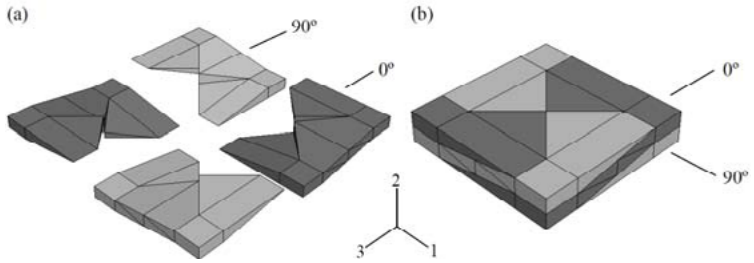


**Figure 6:** Unit cell model: (a) exploded view and (b) assembled view.
1-direction tows have light shading, and 3-direction tows are dark shaded.

### 4.1 Formulation of the finite element Model

The FE mesh for a single tow, consists of 12 elements: two 8-node brick elements, six 6-node wedge elements, and four 4-node tetrahedral elements. The DLR-XT unit cell model is an assembly of four tow models, Fig.6, bonded together through the fully contacted interfaces. Inevitably, the small number of elements is achieved with some loss of accuracy. The fidelity of the model will be assessed by using the experimental data in Section 4.5.

### 4.2 Modelling of waviness

Waviness in the DLR-XT material and the misalignment angle, $\xi = 7^{o}$, has been measured over a large region of available micrographs; and used to create the material orientation of the tows in the finite element model. Figure 7 shows the fibre directions.

### 4.3 Material properties

Blacklock and Hayhurst [8,10] reported the initial elastic properties and multi-axial failure of the tows. The longitudinal stress strain curve of uni-directional tows were obtained using the physical model of Hayhurst *et al*., [6] and Tang *et al*., [4] and the fracture behaviour by dynamic fibre failure mechanism by instantaneous pullout deactivation due to [8].

### 4.4 Elastic Properties

All the elastic properties used for the finite element model are given in Fig.8. The discretised longitudinal stress-strain curves are shown in Fig.8a, the solid line is for a uni- directional

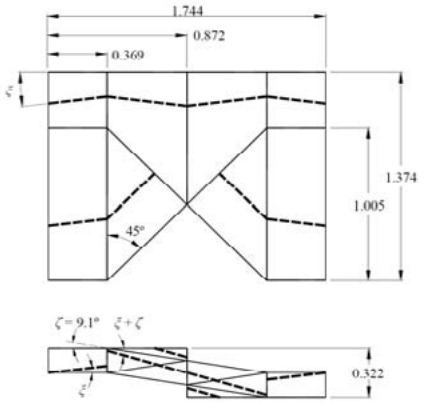


**Figure 7:** Tow waviness: (a) plan view of 1-3 plane and (b) side elevation of 2-3 plane. Misalignment angle is shown as $\xi = 7^{o}$.

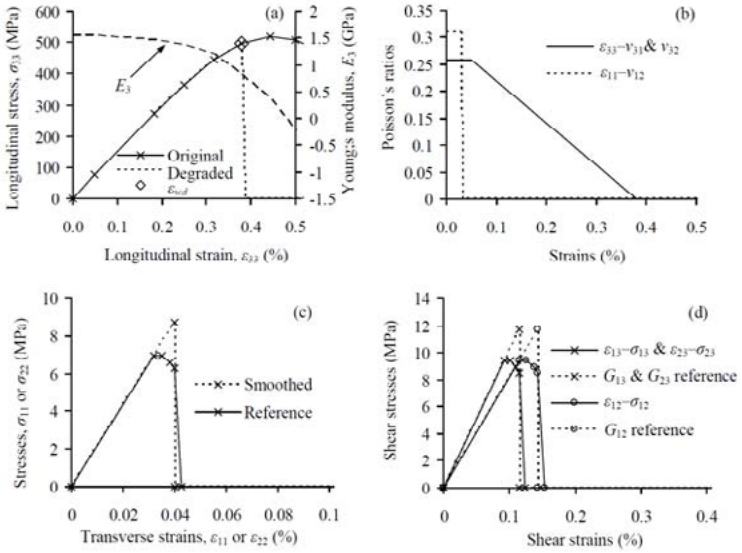


**Figure 8:** Material properties of a uni-directional DLR-XT tow: (a) longitudinal stress-strain curve (b) transverse stress-strain curves (c) Poisson's ratios, $\nu_{12}$, $\nu_{31}$ and $\nu_{32}$ and (d) shear stress-strain curves.

tow under longitudinal straining, and the broken line is the degraded curve, which considers the dynamic fibre failure at $\varepsilon_{33} = \varepsilon_{wd}$. The variation of Poisson's ratios, $\nu_{12}$, $\nu_{31}$ and $\nu_{32}$, with longitudinal strain are shown in Fig.8b. The transverse and shear stress-strain curves, shown in Fig.8c and 8d, are smoothed around the peaks of the curves.

### 4.5 Predictions

Using the FE-based multi-linear elastic model and the material properties in Fig.8, two predictions are made for $\xi$ = 0º and 7º as defined in Section 4.2. Fig.9 shows a comparison between the predictions and experimental data [5]. The effects of tow waviness on the stiffness of the stress-strain curves are significant. The model $\xi$ = 0º predicts a higher stiffness, and failure stress, but a lower failure strain than for $\xi$ = 7º. In comparison with the experimental data, only the prediction for $\xi$ = 7º, correlates well with experimental data. Hence the effect of tow waviness on the strength and fracture strain is significant.

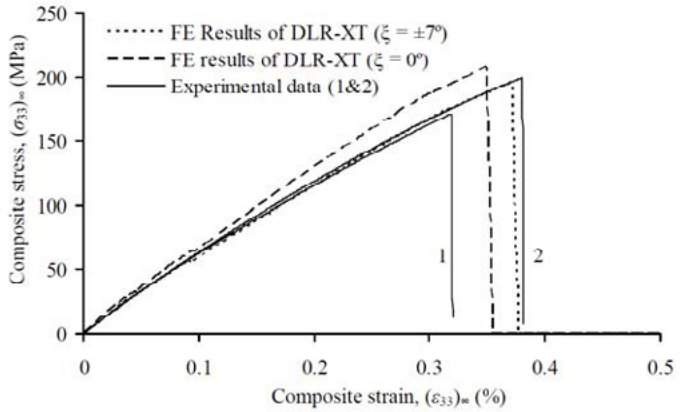


**Figure 9:** Comparison between predicted stress-strain curves and experimental data for a plain weave DLR-XT laminate.

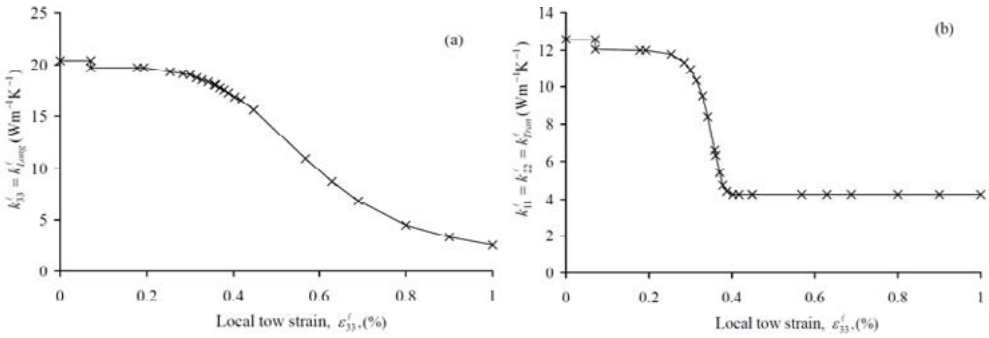


**Figure 10:** Thermal material properties of a uni-directional DLR-XT tow, and discretised crosses: (a) longitudinal thermal conductivity-strain curve; and (b) transverse thermal conductivity-strain curve.

## 5 THERMAL BEHAVIOUR OF A UNI-DIRECTIONAL CMC TOW

FE analysis has been done using coupled stress-thermal-strain strain data.

### 5.1 Tow longitudinal thermal conductivity

Tang *et al*.[4] showed that the longitudinal thermal conductivity is controlled by the air gaps introduced on matrix cracking and fibre failure. They derived equations, based on the thermo-mechanical properties of the constituent materials, which can be numerically integrated to produce variations of the local tow longitudinal thermal conductivity, $k_{Long}^{\ell}$, with local tow strain, $\varepsilon_{33}^{\ell}$. The relevant equations for variation of $k_{Long}^{\ell} \big/ k_{Long}^{\ell-Initial}$ with the tow damage variable $\omega$ and for the variation of $k_{Long}^{\ell} \big/ k_{Long}^{\ell-Initial}$ with $\varepsilon_{33}^{\ell}$ are obtained by coupled numerical integration of the governing equations [4]. Using these relations, and values of $k_{Long}^{Initial}$, the variation of $k_{Long}^{\ell}$ with $\varepsilon_{33}^{\ell}$ have been obtained from the base material parameters and are given in Fig.10a. An initial value of $k_{Long}^{Initial} = k_{33}^{\ell} = 20.38$ $Wm^{-1}K^{-1}$ has been used to determine Fig.10a, shown discretised as multi-linear curves using typically 25 data crosses.

The first step reduction in $k_{Long}^{\ell}$ shown in Fig.10a is due to matrix cracking and the subsequent monotonic decrease that results from fibre failure. The data in Fig.10a is used as the discretised multi-linear materials input data for the finite element model.

### 5.2 Tow transverse thermal conductivity

Tang *et al*. [4] have shown that the degradation of transverse thermal conductivity is controlled by the process of wake debonding, Fig.2d, which produces a cylindrical air gap at the interface between fibre and matrix in a block of material associated with a single fibre located between two adjacent matrix cracks. Poor transverse thermal conductivity of the cylindrical air gap prevents transverse heat flow through the fibre and some of the matrix. The degradation of the local transverse thermal conductivity, $k_{Tran}^{\ell}$, with local tow strain, $\varepsilon_{33}^{\ell}$, is related to the ratio, $N/N_T$. The variation of $k_{Tran}^{\ell} \big/ k_{Tran}^{\ell-Initial}$ with $\varepsilon_{33}^{\ell}$ has been determined from Tang e*t al* [4]; with $k_{Tran}^{\ell-Initial} = k_{11}^{\ell} = k_{22}^{\ell} = 12.56$ $Wm^{-1}K^{-1}$. The graph of $k_{Tran}^{\ell}$ against $\varepsilon_{33}^{\ell}$ is given in Fig.10b, which is used in the FE analysis discretised by 25 data crosses.

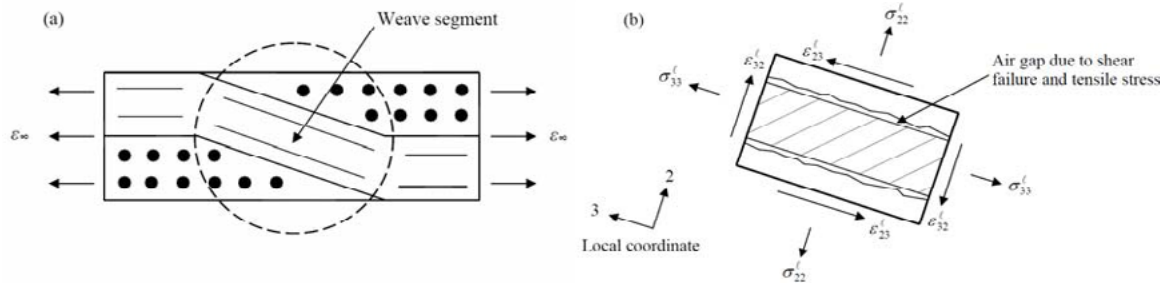


**Figure 11:** Schematic:(a) a woven unit cell under longitudinal straining; and (b) element within the circled weave segment showing interface damage as a result of shear failure and tensile stress.

### 5.3 Effect of shear strain on the longitudinal and through-thickness thermal conductivity

In the composite weave section, Fig.11a. stress and strain components are defined in the local coordinate system, where $\sigma_\infty$ and $\varepsilon_\infty$ are the global remote stress values. Failure of the fibre/matrix interface is shown in Fig.11b due to local shear and normal stress. When $\varepsilon_{32}^{\ell}$, is greater than the critical failure strain, $\varepsilon_{32}^{fs}$, the continuity of the fibre-matrix interface is broken and partial failure is assumed. The partial failure affects the mechanical behaviour, but the thermal response is unchanged since the failure surfaces are in contact. If the normal stress, $\sigma_{22}^{\ell}$, is less than a small positive lower level, $\sigma_{22}^{\ell L}$, i.e. $\sigma_{22}^{\ell} < \sigma_{22}^{\ell L}$, the fibres and matrix are assumed to be in sufficient contact for heat transfer to take place. However, when $\sigma_{22}^{\ell} > \sigma_{22}^{\ell L}$, an air gap is assumed to form, and transverse heat transfer is prevented. The effects of a through-thickness shear failure condition, $\varepsilon_{32}^{\ell} > \varepsilon_{32}^{fs}$, and $\sigma_{22}^{\ell} > \sigma_{22}^{\ell L}$ on transverse conductivity are assumed to dominate over the effects of wake debonding that results in the separation of the two surfaces on the failure plane due to $\sigma_{33}^{\ell}$. The following mechanisms will be considered: (i) Wake debonding driven by longitudinal tension $\sigma_{33}^{\ell}$; or (ii) Shear failure induced by shear or transverse tension, $\varepsilon_{32}^{\ell} > \varepsilon_{32}^{fs}$, with $\sigma_{22}^{\ell} > \sigma_{22}^{\ell L}$.

## 6 FORMULATION OF THE FINITE ELEMENT MODEL

The coupled thermal-mechanical stress model reported here has been formulated using strain dependent thermal material properties, Fig.10. The details of the formulation for mechanical behaviour are given in earlier sections, and can also be found in Zhang and Hayhurst [7]. The formulation of the model for thermal behaviour is now addressed [11].

### 6.1 Heat flow in a homogenised uni-directional tow

A heterogeneous uni-directional tow or lamina was homogenised to a single block e.g. Fig.2a. For the present three dimensional steady-state heat conduction problem, there are three independent tow thermal conductivities: $k_1$, $k_2$, and $k_3$, defined relative to the local tow axes given in Fig.2a. For anisotropic continua the steady-state heat conduction equation is given by Fourier's law, particularised for composites by White and Knutsson [12].

$$\begin{Bmatrix} q_1 \\ q_2 \\ q_3 \end{Bmatrix} = -\begin{bmatrix} k_{11}^{\ell} & 0 & 0 \\ 0 & k_{22}^{\ell} & 0 \\ 0 & 0 & k_{33}^{\ell} \end{bmatrix} \begin{Bmatrix} \partial T/\partial x_1 \\ \partial T/\partial x_2 \\ \partial T/\partial x_3 \end{Bmatrix} \tag{2}$$

where $q_i$ is the heat flux; $k_{ij}$ the thermal conductivity; and $\partial T/\partial x_i$ the thermal gradient ($i, j$=1, 2, 3). In local coordinates, c.f. Fig.2a, $k_{33}^{\ell}$ is the thermal conductivity along the tow, $k_{22}^{\ell}$ is the out-of-plane (through-thickness), and $k_{11}^{\ell}$, is the in-plane transverse to tow.

### 6.2 Determination of Unit Cell Heat Flux

To perform the unit cell FE analyses the discretised multi-linear curves of Fig.10 were used. Mechanical straining in the 3-direction, c.f. Figs.2a and 6, was imposed in terms of the boundary displacements as a succession of small strain increments; and over each increment the mechanical-thermal problem was solved for a unity thermal gradient between the upper an lower surfaces of the unit cell. For each strain increment, element thermal conductivities were evaluated by ABAQUS from Fig.10 using the mechanical strain fields at the start of the increment; and these values were used to compute heat flux (Watts $m^{-2}$) at nodes over the unit cell lower face, at the end of the current strain increment. These local values were integrated over the lower surface to determine the total heat flux, to give the transverse thermal conductivity of the unit cell, since a unity thermal gradient boundary condition was imposed.

### 6.3 Implementation of Subroutine USDFLD in ABAQUS, SIMULIA, [9]

The present thermo-mechanical model has been implemented using the FE package, ABAQUS/standard and a user defined subroutine, USDFLD. The discretised strain dependent tow thermal conductivities, c.f. Fig.10 have been defined as functions of the strain field variables in the input file. For each increment, the subroutine USDFLD read the local strains at each integration point and defined the tow thermal conductivity properties. Automatic incrementation algorithms and the increment redefinition variable, PNEWDT, defined in ABAQUS, were continuously updated to ensure that values of the field variables at the end of the relevant strain increments were located exactly at the discretised points of Fig.10.

## 7 THERMAL CONDUCTIVITY-STRAIN RESPONSE OF DLR-XT COMPOSITE

### 7.1 Formulation of the finite element Model

The mesh and geometry of the DLR-XT unit cell model is exactly as described in Section 4.1 for the model used in the mechanical analysis. The fidelity of the model for thermal flux is assessed by comparison with experimental data in Section 7.2.

Periodic displacement boundary condition was applied to the unit cell to simulate a uni-axial strain along the 0º tow direction. Steady state heat conduction was modelled by a unity thermal gradient between the top and bottom faces of the unit cell, all other faces were lagged.

### 7.2 Predicted thermal response

For the materials tested by Sheikh *et al*. [5], no results were obtained for in-plane composite thermal conductivity, and no attempt was made to predict in-plane thermal

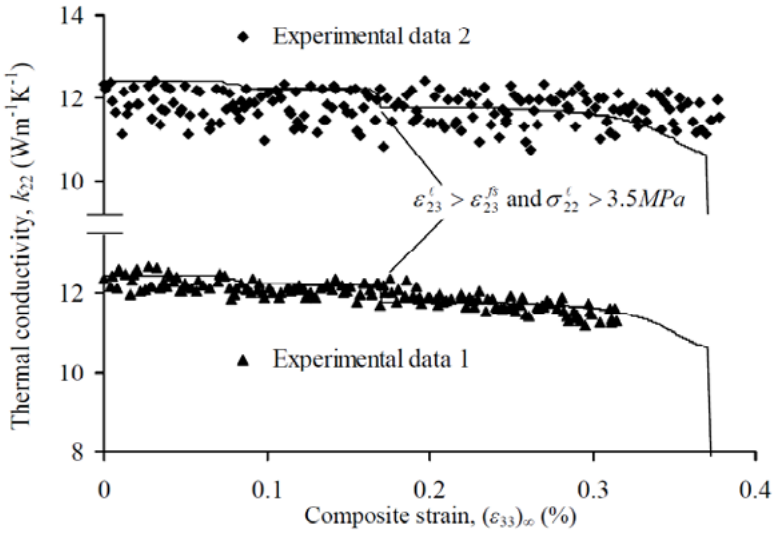


**Figure 12:** Predicted through-thickness thermal conductivities for DLR-XT ($\xi = \pm 7^{o}$) with effects of shear failure when $\varepsilon_{23}^{\ell} > \varepsilon_{23}^{fs}$ and $\sigma_{22}^{\ell} > 3.5MPa$ .

conductivities. Predictions of the variation of composite transverse thermal conductivity, $k_{22,}$ with strain, $(\varepsilon_{33})_{\infty}$, are given in Fig.12 for $\xi = \pm 7^{o}$ with consideration of shear strain failure. The shear failure mechanism, introduced in Section 2.3 is assumed to be triggered when the transverse stress exceeds a lower bound, $\sigma_{22}^{\ell} > \sigma_{22}^{\ell L}$. Since no data is available for $\sigma_{22}^{\ell L}$, it has been determined by best fitting to experimental data, and a value of $\sigma_{22}^{\ell L}$=3.5 MPa wasdetermined. The curve for $\xi = \pm 7^{o}$ in Fig.12 predicts the experimental data well.

Closer examination of the prediction in Fig.12 shows a sharp drop in the curve at $(\varepsilon_{33})_{\infty} \approx 0.17\%$. This is due to the shear failure mode being activated, $\varepsilon_{23}^{\ell} > \varepsilon_{23}^{fs} = 0.1152\%$ and overriding the reduction in thermal conductivity due to wake debonding [11]. Therefore, the plain weave DLR-XT has its out-of-plane transverse thermal conductivity actively reduced by the shear failure mechanism, coupled with a waviness angle of $\xi = \pm 7^{o}$.

## 8 CONCLUSIONS

Mechanical response: for the two levels of waviness considered $\xi = 0^{o}$ and $7^{o}$, the effect of increased waviness is to increase flexibility and increase failure strains. The predicted stress-strain curves for $\xi = \pm 7^{o}$ agree best with experimental results.

Thermal Response: with inclusion of failure due to out-of-plane shear very good predictions of the composite transverse thermal conductivity-strain curve have been achieved with waviness $\xi = \pm 7^{o}$. Hence thermal conductivity degradation takes place by out-of-plane shear, and by the wake debonding that accompanies fibre failure.

The coupled computational algorithm has successfully and accurately predicted both the mechanical and thermal responses of the DLR-XT Ceramic Matrix Composite.

## 9 REFERENCES

[1] Marshall, D. B. and Cox, B. N. Integral textile ceramic structures. *Annu. Rev. Mater. Res*., (2008) **38**, 425–443.
[2] Evans, A. G. & Naslain, R. High-temperature ceramic-matrix composites. *Ceram. Trans*. (1995) **57**, 381–388.
[3] McGlockton, M. A., Cox, B. N. and McMeeking, R. M., A binary model of textile composites: III high failure strain and work of fracture in 3D weaves *Acta Metall. Mater*. (2003) **51,** 1573 – 16
[4] Tang, C., Blacklock, M, and Hayhurst, D. R. Uni-axial stress-strain response and thermal conductivity degradation of ceramic matrix composite fibre tows. *Proc. R. Soc. A*, (2009) **465**, 2849–2876.
[5] Sheikh, M. A., Taylor, S. C., Hayhurst, D. R. and Taylor, R. Experimental investigation of the effect of mechanical loading on thermal transport in ceramic matrix composites. (2009) *J. Multiscale Model.* **1,** 3.
[6] Hayhurst, D. R., Leckie, F. A. and Evans, A. Component design-based model for deformation and rupture of tough fibre-reinforced ceramic matrix composites. *Proc. R. Soc. Lond. A*. (1991) **434**, 369–381.
[7] Zhang D, Hayhurst DR. Stress-strain and fracture behaviour of 0/90 and plain weave ceramic matrix composites from tow multi-axial properties *Int, J of Solids and Structures,* (2010) **47,** 2958-2969
[8] Blacklock, M, and Hayhurst, D. R., Multi-axial failure of Ceramic Matrix Composite fibre tows', J. Applied Mech., (2011) **78**, 031017-1 - 031017-10.
[9] SIMULIA. ABAQUS user's manual. (2006) Version 6.6. Providence, Rhode Island, US.
[10] Blacklock, M, and Hayhurst, D. R., Initial Elastic Properties of Ceramic Matrix Composite Fibre Tows, J. Applied Mech., (2012) **79**, 051020-1- 051020-11.
[11] Zhang D, Hayhurst DR. Influence of applied in-plane strain on travsverse termal conductivity of 0/90 and plain weave ceramic matrix composites *Int, J of Solids and Structures,* (2011) **48,** 828-842.
[12] White, J.L. e and Knutsson, A. Theory of thermal conductivity, heat conductionand convective heat transfer in fiber filled polymer composites, *Polymer Engng Rev.* (1982) **2** (1) pp. 71–82.